

Application of vibrational correlation formalism to internal conversion rate: Case study of Cu_n ($n = 3, 6$, and 9) and H_2/Cu_3

Sandro Giuseppe Chiodo, and Tzonka Mineva

Citation: *The Journal of Chemical Physics* **142**, 114311 (2015); doi: 10.1063/1.4915127

View online: <https://doi.org/10.1063/1.4915127>

View Table of Contents: <http://aip.scitation.org/toc/jcp/142/11>

Published by the American Institute of Physics

Articles you may be interested in

[Time-dependent approaches for the calculation of intersystem crossing rates](#)

The Journal of Chemical Physics **134**, 154105 (2011); 10.1063/1.3575582

[Calculation of internal conversion rate constants of single vibronic levels in \$S_1\$ benzene](#)

The Journal of Chemical Physics **101**, 6632 (1994); 10.1063/1.468457

[Investigation of finite-size effects in chemical bonding of AuPd nanoalloys](#)

The Journal of Chemical Physics **143**, 144309 (2015); 10.1063/1.4932685

[Theoretical study of radiative and non-radiative decay processes in pyrazine derivatives](#)

The Journal of Chemical Physics **135**, 014304 (2011); 10.1063/1.3606579

[First-principles study of Au–Cu alloy surface changes induced by gas adsorption of CO, NO, or \$\text{O}_2\$](#)

The Journal of Chemical Physics **145**, 024701 (2016); 10.1063/1.4955104

[Vibronic coupling in molecular crystals: A Franck-Condon Herzberg-Teller model of H-aggregate fluorescence based on quantum chemical cluster calculations](#)

The Journal of Chemical Physics **143**, 114116 (2015); 10.1063/1.4930606



Application of vibrational correlation formalism to internal conversion rate: Case study of Cu_n ($n = 3, 6$, and 9) and H_2/Cu_3

Sandro Giuseppe Chiodo and Tzonka Mineva^{a)}

Institut Charles Gerhardt Montpellier, CNRS/ENSCM/UM1/UM2, 8 rue de l'Ecole Normale, 34296 Montpellier Cédex 5, France

(Received 18 October 2014; accepted 5 March 2015; published online 19 March 2015)

This work reports non-radiative internal conversion (IC) rate constants obtained for Cu_n with $n = 3, 6$, and 9 and H_2 on Cu_3 . The Time-Dependent Density Functional Theory (TDDFT) method was employed with three different functionals in order to investigate the electronic structures and the absorption spectra. The performance of the generalized gradient approximation of Perdew, Burke and Ernzerhof (PBE) and the hybrid B3LYP and PBE0 exchange correlation functionals in combination with the SVP and the def2-TZVP basis sets was examined. TDDFT results were used as input data to compute internal conversion rate constants. For this purpose, we have developed a program package. A description of the theoretical background used in our numerical implementation and the program input file is presented. In view of future applications of this program package in photoinduced catalysis, we present the analysis of the IC rate processes for the photodissociation of H_2 on Cu_3 . These results showed the applicability of the method and the computational program to identify the vibrational modes in transition metal clusters giving rise to the largest IC rate constant due to their interactions with the excited electronic states occurring in the hot-electron induced dissociation phenomena. © 2015 AIP Publishing LLC. [<http://dx.doi.org/10.1063/1.4915127>]

INTRODUCTION

Understanding the optical processes in noble metal nanoparticles is of both applied^{1–10} and fundamental^{11–20} interests. From the applied point of view, the successful use of large noble metal nanoparticles is due to the generation of the so-called “hot electrons” in the conduction band by an optical excitation in resonance with the plasmon band. This is in the basis of a range of interesting applications as for instance in photothermal therapy,²¹ where the laser excitation is employed to kill or damage cancer cells or in catalysis, where photoexcitation of metal-nanoparticle is responsible for their catalytic reactivity. From the fundamental point of view, the photophysics evolution of large to small particles (<2 nm) has attracted a considerable interest in the recent years. Whereas the optical features in large particles were found very similar to their bulk counterparts, in clusters of few or few tens of atoms, molecular-like properties was reported.^{16,18,22} For example, in the spherical gold nano-structures, the localized surface plasmon resonance, a collective oscillation of the conduction electrons, occurs at the visible to near UV region of the spectrum. The absorption of light in small clusters containing up to 55 Au atoms is found different, showing discrete features in the transient optical spectra and relatively longer relaxation time of the excited electrons due to their interaction with the photons.

Smaller particles are less investigated mainly because of the difficulties to stabilize them. These particles start to be accessible to the experiment with the developments of

novel synthesis routes for sub-nanoparticles preparation in the matrices of inert gases²³ or in the pores of zeolitic microporous materials.²⁴ Presently, the detailed description of the photophysical processes in small metallic clusters (<2 nm) with larger band gap and localized molecular orbitals is still limited, despite the general consensus that the optical behavior of clusters with 10–55 atoms is more likely similar to the optical response in molecules. Most of the studies using femtosecond laser spectroscopy to measure the electron relaxation dynamics, which is dominated by the electron phonon interaction, reported a significantly slower relaxation time (in the ps and ns scales) in the smaller clusters compared to the fs relaxation time in large particles and in the bulk materials.^{13,16,18,22}

Among various metals, gold and silver nanoparticles have been the mostly studied ones. Other metals should, in theory, show plasmon resonances belonging to the UV-vis-NIR region,^{25,26} but they are unstable and difficult to handle because their surfaces may undergo oxidation which widely influence the optical properties. Concerning the Cu nanoparticles, it was demonstrated that their absorption spectra are different from those of Ag and Au.²⁰ The surface plasmon in copper is strongly damped by the s-d hybridization and interband transitions occurring at the similar energy,^{27,28} whereas in gold and silver, an intensive and narrow plasmon occurs followed by a well separated interband transitions at higher energies. More precise optical spectra of mass selected Cu-clusters with 1–9 atoms exhibit a larger number of transitions in comparison to the similar size of silver particle.²³ Radiative and non-radiative relaxation processes were suggested as channels being pertinent to the phenomenon of photoinduced diffusion and aggregation of Cu atoms in rare gas matrices by measuring and analyzing UV-visible absorption, fluorescence emission, and

^{a)} Author to whom correspondence should be addressed. Electronic mail: tzonka.mineva@enscm.fr

excitation spectra of Cu clusters up to pentamer in solid Xe at 12 K temperature.²⁹

The theoretical background to explain the photophysics of large noble nanoparticles was developed by Mie,³⁰ based on the classical Maxwell electrodynamics. This classical model uses as input parameters the dielectric constant of the metal particle and the surroundings. Subsequently, this approach was extended to better approximate the frequency dependent dielectric constants using the Drude model of free electron gas and to account for the spherical or cylindrical shape of the particle. For exhaustive reviews, we point to the works of Link and El-Sayed,³¹ and of Hartland.²² For smaller clusters, this classical picture is no longer applicable because of the localization of the electron states and the molecular-like behavior of the clusters. It would be thus more relevant to apply quantum mechanical (QM) models that have been developed and applied with various successes to describe the vibrational structure of the absorption spectra and nonradiative decay processes in organic molecules. The electron transitions are mostly theoretically approached by the use of *ab-initio* methods based on density functional theory and in particular its time-dependent extension, time-dependent density functional theory (TDDFT). The transition moments and the vibrational energies obtained at the (TD)DFT levels are now used in several algorithms. Without making an extensive review of this intensively developing branch of theoretical methods using as inputs the electronic transition moments and vibrational energies from the first principle DFT, we refer to the recent computational schemes^{32–44} that were proposed to quantify the electronic-vibrational interactions, vibronic spectra, and to compute the radiative or nonradiative rate constants within the harmonic approximation level, while taking into account the Franck-Condon,^{45–48} Herzberg-Teller,⁴⁹ and Duschinsky mixing effects.⁵⁰

The non-radiative transition rate in polyatomic organic molecules has been successfully computed in the frame of path integral formalism,^{41–44} and we found it relevant to adopt and extend it to selected copper clusters. In the present work, we applied the vibrational correlation formalism to compute the internal conversion rate constants for minima structures of neutral copper clusters Cu_n (n = 3, 6, 9) (see Figure 1). A more thorough understanding of this effect requires an accurate analysis of the electronic structure of the metal nanoparticles and of their absorption spectra and, consequently, the study of the nonradiative processes, i.e., the study of the internal conversion (IC). In the internal conversion processes, the electronic excitation energy is transformed into the vibrational energy of the electronic ground state, which involves vibronic coupling, i.e., an electron-nuclear vibration interaction. If this interaction is large in electron-transporting materials, the dissipation of the energy should be large because the hopping electron couples strongly with intramolecular vibrations.⁵¹

The manuscript is organized as follows: first, the basic concepts of the theoretical background, proposed by Niu *et al.*,^{41–44} is briefly outlined, followed by a more detailed description of its numerical implementation that we have realised in order to compute in an efficient and automated way the internal conversion rate constant. In the section on “Results and Discussion,” the analysis of the electronic structures of the

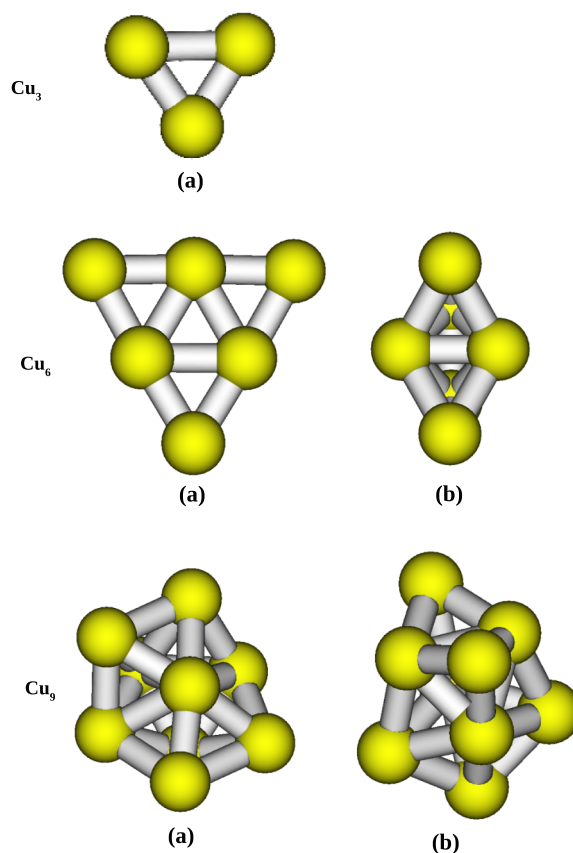


FIG. 1. Geometries of the calculated Cu₃, Cu₆, and Cu₉ clusters. They refer to the ground state for each level of theory.

Cu_n (n = 3, 6, and 9) clusters and their computed absorption spectra is presented while carefully examining the effect of the exchange-correlation functional and basis sets. For the Cu₃ ground-state cluster, EOM-CCSD/SVD method was applied in order to compare with the DFT results. Further on, our study on the IC processes in the copper clusters and in the H₂ photoinduced dissociation on Cu₃ cluster is presented.

THEORY AND COMPUTATIONAL DETAILS

Theory

In this section, we will outline briefly the relevant part of the theory used referring to the detailed discussions in the original papers.^{41–44} The method to derive the temperature dependent IC rate constant is based on the path integrals of Gaussian type correlation function, originally proposed by Pollak *et al.*^{38,52–54} and further developed by Tang *et al.*⁵⁵ and Niu *et al.*^{41–44} This formalism is a promoting-mode free rate containing Duschinsky rotation effect, so the mixing of the vibrational modes is explicitly considered and the method is fully analytic. In this context, the spontaneous emission rate can be evaluated, according to the Fermi's golden rule, starting from the following general expression:

$$k_{ic}(T) = \frac{2\pi}{\hbar} \sum_{\nu_i \nu_f} P_{i\nu_i}(T) |H'_{\nu_f \nu_i}|^2 \delta(E_{if} + E_{i\nu_i} - E_{f\nu_f}), \quad (1)$$

where

$$P_{iv_i} = \prod_k \frac{e^{-\beta E_{iv_{ik}}}}{\sum_{v_k=0}^{\infty} e^{-\beta E_{iv_k}}} = \frac{e^{-\beta E_{iv_i}}}{Z_{iv}} \quad E_{iv_{ik}} = (v_{ik} + 1/2)\hbar\omega_{ik}, \quad (2)$$

and $\delta(E_{if} + E_{iv_i} - E_{fv_f})$ is the Dirac-delta function. Notice that i and f subscript indices refer to the final and initial state, respectively. The v_{ik} and ω_{ik} are the vibrational quantum numbers and frequencies of the first state, respectively. H'_{vfv_i} are the matrix elements of the Born-Oppenheimer term H' , which, using the Condon approximation, can be written as

$$H'_{vfv_i} = \sum_l \langle \Phi_f | \hat{P}_{fl} | \Phi_i \rangle \langle \Theta_{fv_f} | \hat{P}_{fl} | \Theta_{iv_i} \rangle. \quad (3)$$

Here, $\hat{P}_{fl} = -i\hbar(\partial/\partial Q_{fl})$ is the mass-weighted normal momentum operator and Q_{fl} is the l th normal mode coordinate of the final state. $|\Phi_i\rangle$ and $|\Theta_{iv_i}\rangle$ are the electronic and vibrational mode wavefunctions of the initial state, respectively. By combining the Eq. (1) with the Eq. (3), the k_{ic} becomes

$$k_{ic} = \frac{2\pi}{\hbar} \sum_{lk} \frac{R_{lk}^f}{Z_{iv}} \sum_{v_{iv_f}} e^{-\beta E_{iv_i}} P_{lk}^f \delta(E_{if} + E_{iv_i} - E_{fv_f}), \quad (4)$$

with

$$R_{lk}^f = \langle \Phi_f | \hat{P}_{fl} | \Phi_i \rangle \langle \Theta_{iv_i} | \hat{P}_{fk} | \Theta_{fv_f} \rangle, \quad (5)$$

$$P_{lk}^f = \langle \Theta_{fv_f} | \hat{P}_{fl} | \Theta_{iv_i} \rangle \langle \Theta_{iv_i} | \hat{P}_{fk} | \Theta_{fv_f} \rangle.$$

Applying the Fourier transformation to the Dirac-delta function, the final expression of k_{ic} is

$$k_{ic} = \frac{1}{\hbar} \sum_{lk} R_{lk}^f \int_{-\infty}^{\infty} \frac{\rho_{lk}^f(\tau_f, \tau_i)}{Z_{iv}} e^{iE_{if}\tau} d\tau, \quad (6)$$

with $\tau_f = \tau$, $\tau_i = -i\beta - \tau$, and $\tau = t/\hbar$. E_{if} is the electronic transition energy. The derivation of the thermal vibration correlation function, $\rho_{lk}^f(\tau_f, \tau_i)$ in the above equation is described in details in the original papers of Niu *et al.*^{41–44}

Using the expansion to the lowest order in perturbation theory, the vibronic coupling term of the electronic part R_{lk}^f is written as

$$\langle \Phi_f | \hat{P}_{fl} | \Phi_i \rangle = -i\hbar \frac{\langle \Phi_f^0 | \partial V / \partial Q_{fl} | \Phi_i^0 \rangle}{E_i^0 - E_f^0}, \quad (7)$$

where Φ_i^0 and Φ_f^0 are the electronic wavefunctions of the initial and final state, respectively, computed over the geometry of the final state (ground state). E_i^0 and E_f^0 are the corresponding energies.

The non-adiabatic coupling (NAC) matrix elements in expression (7) were computed according to the work of Send and Furche.⁵⁶ Cartesian NAC vectors were calculated with the TURBOMOLE V6.4⁵⁷ code and transformed as

$$\frac{\langle \Phi_f^0 | \partial V / \partial Q_{fl} | \Phi_i^0 \rangle}{E_i^0 - E_f^0} = \sum_{\alpha j} \frac{1}{\sqrt{M_{\alpha}}} L_{fl\alpha j} \frac{\langle \Phi_f^0 | \partial V / \partial \xi_{f\alpha j} | \Phi_i^0 \rangle}{E_i^0 - E_f^0}, \quad (8)$$

where the $L_{fl\alpha j}$ is the α -nucleus mass-reduced displacement of the l th mode. M_{α} is the mass of the α nucleus.

Computational details

For all density functional (DF) calculations, the TURBOMOLE V6.4⁵⁷ suite of programs was used. Gaussian-type-orbital SVP⁵⁸ ([7s5p5d]/[6s3p2d]) and def2-TZVP basis sets⁵⁹ ([17s11p7d1f]/[6s4p4d1f]) as implemented in this code were chosen. A large grid for numerical quadrature (“grid 4” option) was employed and a tight SCF convergence criterion of 10^{-8} was selected. To investigate the performance of the exchange correlation functionals, as far as concerns the description of the electronic structure of Cu_n ($n = 3, 6$, and 9) clusters, the generalised gradient approximation (GGA) of Perdew, Burke and Ernzerhof (PBE)⁶⁰ and the two hybrid B3LYP^{61,62} and PBE0⁶³ functionals were used. Restricted and unrestricted MOs for closed and open shell systems, respectively, were employed. No constraints were imposed to retain a specific symmetry during the SCF cycles. The excited states were treated at the TDDFT level and their equilibrium geometries and frequency calculations were carried out only at the B3LYP/SVP level. For that concerning the vibrational analysis, the force constant was evaluated numerically with the NumForce tool.

For the comparison with the experimental spectra, the intensity of the vertical excitations of the computed ones was broadened by using Lorentzian functions with a constant half-width of 0.1 eV.

In specifying the procedure to analyze the IC rate process, a set of vertical excitations was selected for each cluster from those computed only at the B3LYP/SVP level. In this case, the frequencies were scaled by an aptly chosen factor (0.9614), as suggested by Koch and Holthausen⁶⁴ and according to the reference work of Shuai *et al.*⁴²

The Cartesian NAC vector, the frequencies, and the mass reduced displacements for each mode are provided as input data to our program that computes the IC rate constants. In addition, we have given also the possibility to use the Hessian matrix as input.

RESULTS AND DISCUSSION

Among the various considered geometries and spin multiplicities for Cu_3 , Cu_6 , and Cu_9 clusters, we have established the ground state structures that are reported in Figure 1. Table SII in the supplementary material lists the relative energies of the selected cluster structures investigated in this work.⁷⁴ Their geometries are shown in Figure SII. The spin multiplicity is two for the open-shell Cu_3 and Cu_9 , and one for the closed-shell Cu_6 systems. For the Cu_3 species, all levels of theory give structure (a) as ground state. For Cu_6 , structure (a) is predicted from the PBE/def2-TZVP, B3LYP/SVP, B3LYP/def2-TZVP, and PBE0/def2-TZVP, and structure (b) from the PBE/SVP and PBE0/SVP methods. For Cu_9 , all levels of theory give ground state structure (a) with exception of B3LYP/def2-TZVP. This method predicts structure (b). The results reported in Table SII (supplementary material⁷⁴) suggest that Cu clusters can exist in various topologies, very closely spaced in energies in agreement with previous studies.^{65–70} It is therefore not surprising that the ground states’ geometries are strongly dependent on the method employed and most

TABLE I. HOMO-LUMO gap in eV computed at different levels of theory. The values refer to the ground state for each level of theory. Their geometries are reported in Figure 1.

	PBE		B3LYP		PBE0	
	SVP	def2-TZVP	SVP	def2-TZVP	SVP	def2-TZVP
Cu ₃	0.16	0.22	1.10	1.26	1.39	1.52
Cu ₆	0.37	1.93	3.10	3.16	1.59	3.46
Cu ₉	0.29	0.33	1.11	1.39	1.33	1.43

likely the low-energy structures co-exist under the experimental conditions. Note that the results and analysis of the electronic structures, the absorption spectra, and the internal rate processes are presented below for the ground state structures obtained by the particular computational method employed.

Electronic structure

At a first place, the influence of the exchange correlation functional and the basis sets on the MOs was examined rationalizing the trend of the HOMO-LUMO gap (Table I) and the density of the state spectra (DOSS) computed with the PBE,

B3LYP, and PBE0 approximations, each of them combined with two different basis sets (see section on Computational details) as shown in Figures SI2.1–SI2.3 in the supplementary material.⁷⁴ The DOSS refer only to the valence and the conduction band, and the range of the plotting includes predominantly the energies of the MOs involved in the vertical excitations. This analysis shows that the energies of the MOs are, on the whole, influenced by the functional choice and the basis set size, as expected. As an example for the valence band of the Cu₃ (this behaviour is common to the all occupied MOs), the energies, ranging approximately from -0.29 to -0.21 hartree at PBE/SVP level, are shifted to the lower values as the size of the basis set increases and the exact Hartree-Fock exchange contribution in the functional increases. At PBE0/def2-TZVP level, this interval goes approximately from -0.32 to -0.25 hartree. As a result, the HOMO-LUMO gap, which is reported in Table I, increases following inversely the trend of the occupied MO energies. This effect is common to the all clusters with the same geometry and characterises the entire electronic structure of these systems. As reported in Table I, for the Cu₉ with geometry (a) (see Figure 1), the HOMO-LUMO gap goes from 0.29 eV (PBE/SVP) to 1.43 eV (PBE0/def2-TZVP) (the range includes the values obtained at all levels of theory except

TABLE II. Mulliken population analysis of the s, p, and d contributions to the HOMO and LUMO. The values refer to the ground state structures for each level of theory. Their geometries are reported in Figure 1.

			PBE		B3LYP		PBE0	
			SVP	def2-TZVP	SVP	def2-TZVP	SVP	def2-TZVP
Cu ₃	α -HOMO	s	0.75	0.84	0.81	0.88	0.81	0.87
		p	0.17	0.13	0.15	0.11	0.16	0.13
		d	0.08	0.03	0.04	0.00	0.03	0.00
	α -LUMO	s	0.73	0.84	0.78	0.88	0.79	0.88
		p	0.20	0.14	0.18	0.13	0.17	0.13
		d	0.07	0.02	0.04	0.00	0.04	0.00
	β -HOMO	s	0.00	0.00	0.00	0.00	0.00	0.72
		p	0.03	0.01	0.02	0.00	0.02	0.04
		d	0.97	0.99	0.98	1.00	0.98	0.23
	β -LUMO	s	0.73	0.83	0.79	0.87	0.79	0.86
		p	0.20	0.14	0.18	0.13	0.17	0.14
		d	0.07	0.03	0.04	0.00	0.03	0.00
Cu ₆	α -HOMO	s	0.59	0.25	0.73	0.78	0.70	0.77
		p	0.17	0.02	0.10	0.08	0.19	0.10
		d	0.24	0.73	0.18	0.14	0.11	0.13
	α -LUMO	s	0.59	0.75	0.72	0.79	0.67	0.77
		p	0.24	0.22	0.23	0.21	0.24	0.21
		d	0.17	0.03	0.05	0.01	0.09	0.01
	β -HOMO	s	0.62	0.70	0.69	0.74	0.67	0.72
		p	0.24	0.20	0.24	0.23	0.25	0.22
		d	0.13	0.10	0.08	0.04	0.08	0.06
Cu ₉	α -HOMO	s	0.56	0.64	0.63	0.78	0.65	0.70
		p	0.31	0.27	0.29	0.20	0.27	0.26
		d	0.14	0.09	0.09	0.01	0.07	0.04
	α -LUMO	s	0.51	0.59	0.64	0.68	0.64	0.70
		p	0.17	0.13	0.18	0.11	0.20	0.16
		d	0.32	0.28	0.18	0.21	0.16	0.14
	β -HOMO	s	0.63	0.71	0.70	0.75	0.69	0.75
		p	0.24	0.20	0.22	0.22	0.24	0.20
		d	0.13	0.09	0.08	0.03	0.07	0.05

B3LYP/def2-TZVP). Note that these values refer to the α HOMO-LUMO gap. Table II lists the s , p , and d contributions of the α and β HOMO, and LUMO obtained from the Mulliken population analysis. Analysis of orbital compositions, using Mulliken population scheme, was found to give accurate description of the orbitals of interest involved in the optical transitions compared to the experimental results.²³

Analysis of these values reveals that the whole set of both α HOMO and LUMO, and the β LUMO of Cu_3 shows a predominant s -type contribution. Instead, the d one is very small. An opposite behaviour is predicted for the β -HOMO values, with the exception of the PBE0/def2-TZVP ones. These last contributions show that the MO is energetically located in a different way, that is the energetic order of the orbitals is not quite consistent with the other level of theory, where the same shape belongs to the s -HOMO. This is more clearly evident from the plot of the considered molecular orbitals in Figure SI3.1 (supplementary material).⁷⁴ For the Cu_6 species, the s character is also predominant in both HOMO and LUMO obtained employing the B3LYP and the PBE0 functional irrespective of the basis set used and of the structures considered. By the comparison of the results obtained for structure (a), Figures SI3.2(b), SI3.2(e), and SI3.2(f) show their similarity in the shape and energetic order. Instead, using the PBE functional with the def2-TZVP basis set, we obtained that the d contribution is the largest one in HOMO. The s -type character affects also the whole trend of the HOMO and LUMO of the Cu_9 cluster and becomes, as for the other species, higher with the hybrid functionals. Analogous considerations remain valid for all the clusters.

Absorption spectra

Absorption spectra of Cu_n ($n = 1-9$) clusters have been reported recently²³ from both experiment and TDDFT calculations. The authors concluded that in the B3LYP/def2-TZVP results, the effect of the d electrons is not properly taken into account using TDDFT. For this reason, further studies are necessary to understand in detail the nature of optical transitions in Cu clusters.

The absorption spectra, obtained by us, are shown in Figures 2–4. In Table SI3 (supplementary material⁷⁴) are listed the

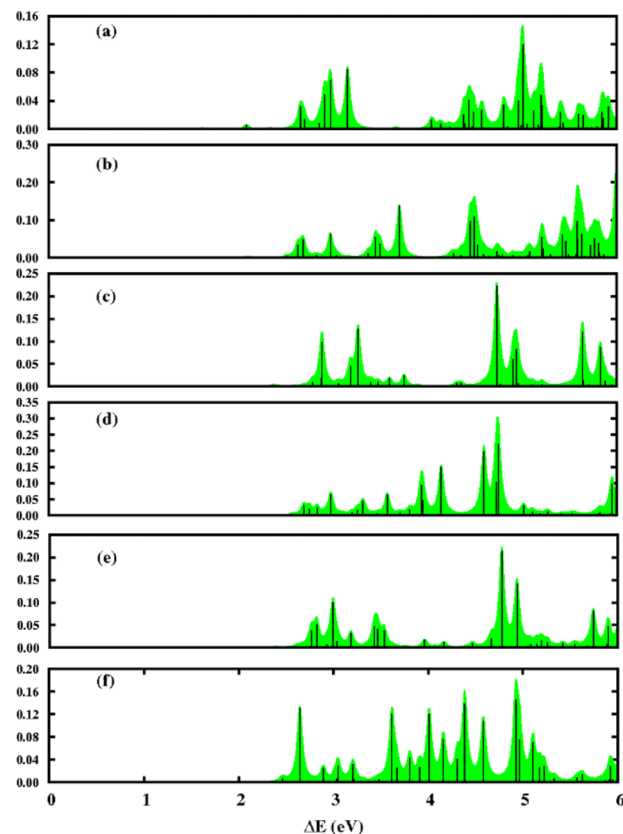


FIG. 2. Absorption spectra for the Cu_3 cluster computed at (a) PBE/SVP, (b) PBE/def2-TZVP, (c) B3LYP/SVP, (d) B3LYP/def2-TZVP, (e) PBE0/SVP, (f) PBE0/def2-TZVP levels of theory. They refer to the ground state structure (a).

electronic excitation energies (ΔE), the oscillatory strengths ($f(r)$), the c^2 weighted coefficients belonging to a given one electron transition, and the corresponding MO excitations. The vertical excitations were selected in the way to belong to the seven most intense peaks. Figures SI3.1–SI3.3 (supplementary material) report graphical representations of the occupied and unoccupied MOs involved in the vertical excitations for each of the computational level employed.⁷⁴ In Table SI3 (supplementary material), we report the excitations, characterised by c^2 coefficients larger than 10% in most of the cases.⁷⁴ At first blush, it can be deduced from the results in Figures 2–4 that

TABLE III. Total s , p , and d contributions (%) involved in the absorption spectra. The values refer to the ground state structures for each level of theory. Their geometries are reported in Figure 1.

Species	PBE						B3LYP						PBE0					
	SVP			def2-TZVP			SVP			def2-TZVP			SVP			def2-TZVP		
Cu_3	s	8.5		40.0	9.0	35.3	11.6		54.6	12.8	50.3	12.2	55.8	14.1	55.4			
	p	2.0	→	55.7	1.3	48.3	1.9	→	42.5	1.4	40.1	2.1	41.4	1.7	36.2			
	d	89.5		4.3	89.7	16.4	86.5		2.9	85.8	9.6	85.7	2.8	84.2	8.4			
Cu_6	s	7.2		45.1	7.5	37.2	8.9		53.5	11.5	55.6	11.1	63.8	11.8	57.7			
	p	2.8	→	48.0	1.3	42.3	1.9	→	42.8	1.5	37.6	3.4	31.3	1.7	35.2			
	d	90.0		6.9	91.2	20.5	89.1		3.7	87.1	6.8	85.5	4.9	86.4	7.1			
Cu_9	s	7.1		46.8	7.0	43.9	9.8		62.6	10.6	55.9	9.8	63.7	10.8	58.8			
	p	3.3	→	45.4	2.0	40.3	3.4	→	31.9	2.3	33.5	3.7	31.4	2.7	31.5			
	d	89.6		7.6	90.8	15.7	86.7		4.9	86.8	10.4	86.3	4.5	86.3	9.5			

these spectra are susceptible to the level of employed theory and, of course, to the geometry used.

An accurate analysis can be done taking into account the total contribution of s , p , and d characters for each spectrum. We have computed this parameter as a weighted average by the c^2 coefficients of the s , p , and d contributions of the MOs involved in each transition and belonging to each excitation, each peak. Then, these values were averaged over the number of peaks from 0 to 6 eV. The MO s , p , and d contributions were obtained by a Mulliken population analysis. These data are collected in Table III. An interesting trend is observed concerning the effect of the approximation used for the exchange correlation functionals. Notice that the data at the left and at the right side of the arrow were computed over the occupied and unoccupied MOs, respectively. They reveal that, irrespective of the considered ground-state geometry, the occupied MOs involved in the excitations have the largest d -contributions using GGA-PBE, compared to B3LYP and PBE0 ones.

Therefore, the conclusion is that the PBE functional favours the transitions from occupied to unoccupied orbitals with larger d character. Increasing the percentage of the exact exchange from B3LYP to PBE0 functionals, the d -contribution in the orbitals involved in the excitations becomes smaller. The opposite situation occurs for the s character. However, in all cases, the transitions go, on average, from MOs where the d character is dominant to MOs where the s and the p contributions are dominant, i.e., transitions $d \rightarrow sp$. For unoccupied

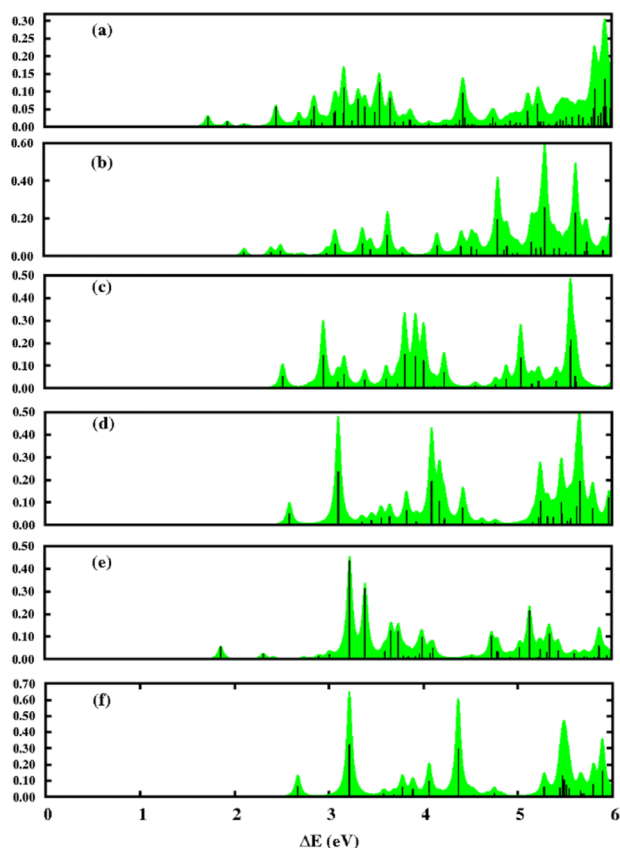


FIG. 3. Absorption spectra for the Cu_6 cluster computed at (a) PBE/SVP, (b) PBE/def2-TZVP, (c) B3LYP/SVP, (d) B3LYP/def2-TZVP, (e) PBE0/SVP, (f) PBE0/def2-TZVP levels of theory. They refer to the ground state structure for each method.

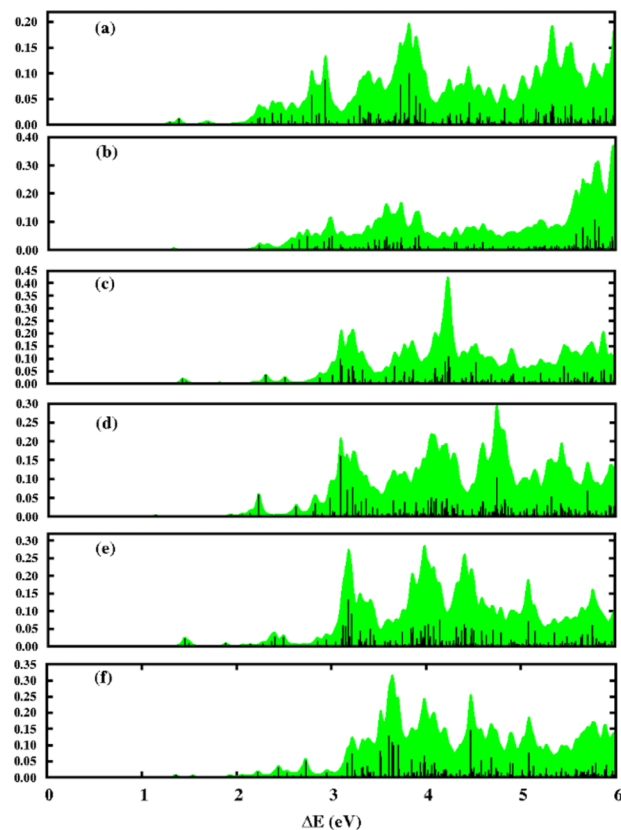


FIG. 4. Absorption spectra for the Cu_9 cluster computed at (a) PBE/SVP, (b) PBE/def2-TZVP, (c) B3LYP/SVP, (d) B3LYP/def2-TZVP, (e) PBE0/SVP, (f) PBE0/def2-TZVP levels of theory. They refer to the ground state structure for each method.

MOs, the d contribution is, instead, increased with the use of the def2-TZVP basis set.

Comparison of the spectra shapes in Figs. 2–4 with the measured absorption spectra²³ shows an overall good agreement, especially for the two hybrid functionals. A very good

TABLE IV. Selected electronic excitation energies (ΔE), oscillatory strengths ($f(r)$), and IC rate constants at 300 K. The values in parentheses are the excitation energies computed after relaxation of the excited state geometry. The values refer to the structures (a) reported in Figure 1.

Species	State N	ΔE (eV)	$f(r)$	k_{ic} (s^{-1})
Cu_3	19	2.47 (2.40)	1.5×10^{-3}	0.7×10^{-2}
	28	2.79 (2.70)	9.8×10^{-3}	0.4×10^{-2}
	53	4.74 (4.72)	2.2×10^{-1}	0.9×10^1
	57	4.91 (4.84)	6.0×10^{-2}	0.1×10^{-2}
	98	5.83 (5.80)	8.7×10^{-2}	0.6×10^1
	156	7.16 (6.92)	4.2×10^{-2}	0.3×10^7
Cu_6	3	2.75 (2.72)	1.3×10^{-6}	0.1×10^9
	4	2.81 (2.77)	4.9×10^{-3}	0.2×10^4
	50	3.81 (3.74)	5.6×10^{-5}	0.4×10^4
	95	4.77 (4.77)	1.8×10^{-2}	0.7×10^1
	111	5.16 (5.16)	2.0×10^{-2}	0.3×10^2
	129	5.42 (5.39)	3.4×10^{-2}	0.1×10^1
Cu_9	143	5.63 (5.62)	2.9×10^{-2}	0.8×10^1
	181	6.36 (6.31)	1.8×10^{-2}	0.1×10^4
	5	1.26 (1.23)	8.5×10^{-9}	0.2×10^7
	20	2.51 (2.51)	2.4×10^{-2}	0.3×10^1

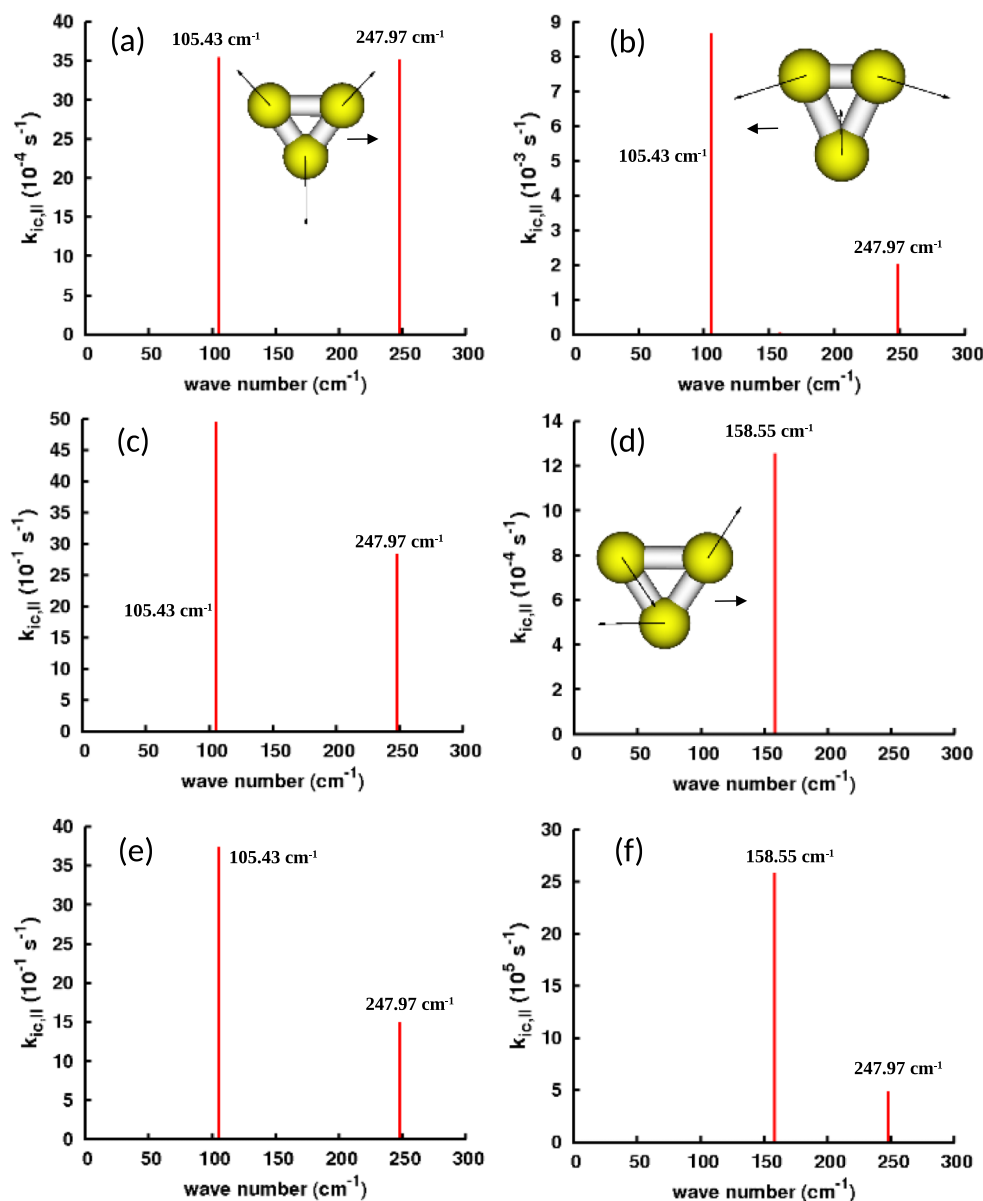


FIG. 5. Diagonal matrix elements of the k_{ic} for the Cu_3 species obtained from the excitations: (a) 19; (b) 28; (c) 53; (d) 57; (e) 98; (f) 156.

agreement is found with the theoretical spectra (using TDDFT with B3LYP/def2-TZVP method) reported in the same work.²³ It is useful to analyze in more details the results obtained at B3LYP/SVP level of theory, which are further used for the interconversion rate constant calculations. The positions of the computed intensive peaks at 2.47, 2.79, 4.74, 4.91, and 5.83 eV in Cu_3 correspond well to the experimental values of 2.66, 2.91, 4.78, 4.94 eV.²³ The observed intense peaks at 3.37 and 3.70 eV were however not identified as intense peaks from the calculations. Similarly, in Cu_6 cluster, there is a good matching between the computed energy positions of the optical transitions and the experimental values.²³ Small intensities were found by the calculations for the experimentally observed well resolved peaks in the 3.1–3.57 eV interval. The strong superposition of the absorption lines in the whole energy range for Cu_9 has not allowed to achieve a good signal to noise ratio.²³ Despite the lack of perfect matching between the theoretical and experimental data in the whole energy regions, the elec-

tronic transitions that are considered in the k_{ic} computations for Cu_3 and Cu_6 agree pretty well with the measured ones. We note also that our test calculations with EOM-CCSD/SVD method for Cu_3 clusters yielded comparable results with those obtained at B3LYP/SVD level of theory. The largest differences between both spectra are in the higher energy range, between 3.2 and 4.8 eV. For example, the well distinguishable intense peaks at 3.31, 3.61, 3.96, and 4.59 eV in the spectrum, computed with EAM-CCSD, correspond to intense peaks, located at 3.27, 3.41, 3.75, and 4.73 eV in the B3LYP spectrum. Comparison with PBE functionals shows that the largest discrepancies are in the range above 4.0 eV, where no intense peaks result from the PBE calculations. Finally, the obtained large number of various minima energy cluster geometries, most probably co-existing at the experimental temperature, suggests that the experimental spectra contain peaks due to optical transitions in several structures and not only in the “ground-state” cluster.

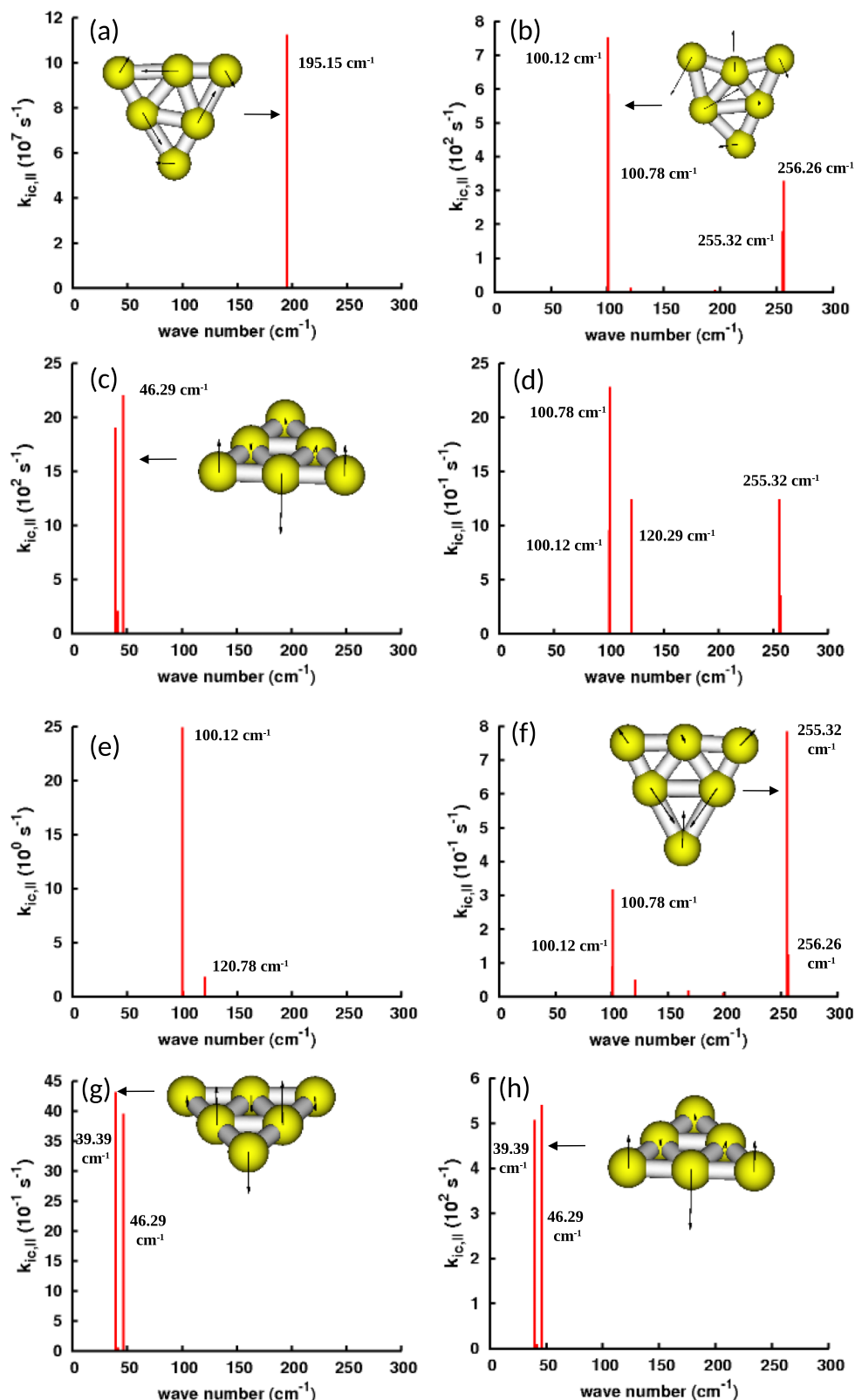


FIG. 6. Diagonal matrix elements of the k_{ic} for the Cu_6 species obtained from the excitations: (a) 3; (b) 4; (c) 50; (d) 95; (e) 111; (f) 129; (g) 143; (h) 181.

Internal conversion processes

Another aspect of this work concerns the discussion of how the structures of Cu clusters affect radiationless transitions of electronic states with the same multiplicity, in-

volving vibronic coupling. To this aim, we have computed the IC rate constant by considering the vibronic coupling for the largest possible energy interval of the optical excitations. Due to the several numerical difficulties to optimize the geometrical structures for every excited state (see section on “Theory and

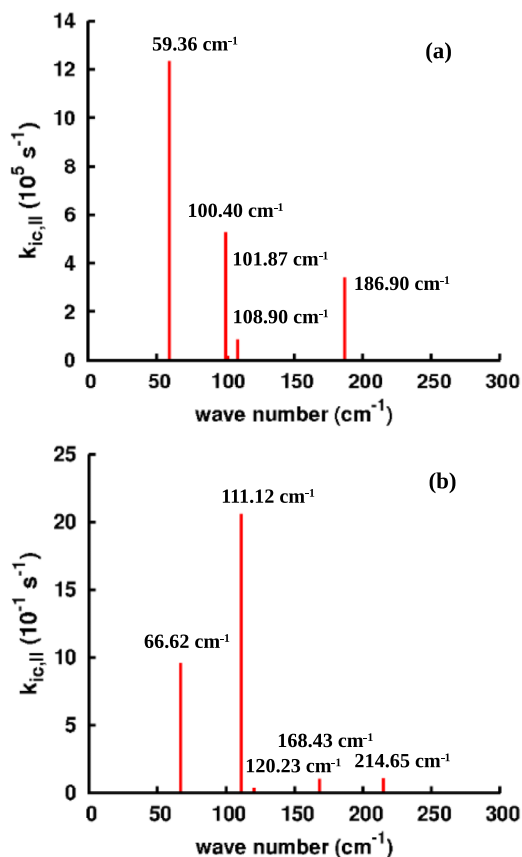


FIG. 7. Diagonal matrix elements of the k_{ic} for the Cu_9 species obtained from the excitations: (a) 5; (b) 20.

Computational Details”) and to compute the IC for the entire spectrum, we have selected a number of peaks depending on the number of optimized excited (final) states’ geometries. Computing k_{ic} requires knowledge about the normal mode coordinates and frequencies of the ground and the excited states’ equilibrium geometries. The k_{ic} values of the studied transitions are collected in Table IV, together with the excitation energies (ΔE) and the oscillatory strengths ($f(r)$). Some of those transitions have not been considered in the previous analysis of the MOs and the optical spectra, since they are characterised by lower $f(r)$ values. The values of ΔE in parenthesis are the excitation energies computed after relaxation of the excited state geometry.

The case of Cu_3 structure will be used to illustrate and discuss the difficulties related to the numerical integration of the correlation functions (ρ_{lk}^f), required for the calculation of the k_{ic} . The main obstacle in this procedure is the fact that the total time interval $[-t, t]$ and the Lorentzian broadening⁴² should be chosen on the empirical basis. Therefore, for the various cases (see below), a total time interval chosen by us varies from $t = 10^9$ fs to $t = 2 \times 10^6$ fs and a Lorentzian broadening from 4×10^{-4} cm⁻¹ to 2×10^{-1} cm⁻¹. In Figure 5 are illustrated the graphical representations of the diagonal matrix elements of the k_{ic} rate, together with the displacement vectors related to each of the Cu_3 vibrational normal modes located at 105.43, 158.55, and 247.97 cm⁻¹. The last value is the frequency of the breathing mode, the symmetric stretching mode. The IC process coupled to the first and last

modes is expected to be very slow as predicted from our k_{ic} values in Figures 5(a)–5(e). The coupling between electronic transitions, corresponding to higher ΔE values, and these vibrational modes become negligible. An internal conversion process in Cu_3 would occur due to the coupling between the asymmetric vibrational mode at 158 cm⁻¹ and the electronic transition with the energy ΔE equal to 7.16 eV, which is not in the UV-vis range. This coupling gives the only significant IC rate constant value of the order of 10^7 s⁻¹. There are two oppositely acting factors contributing to k_{ic} value: a large ΔE contribution tending to decrease k_{ic} from one side and a large geometry displacement from the excited to the ground state leading to an increase of k_{ic} . The displacement of the geometry given by the excitation is, indeed, consistent with the normal mode coordinate displacement because the mode at 158.55 cm⁻¹ is computed to be the most intense one. Thus, this frequency mode is the promoting-mode and there is a small mixture with the breathing mode for Cu_3 cluster. The geometry displacements for the other normal vibrational modes increase (decrease) corresponding to the mode intensity.

In the case of Cu_6 cluster, the k_{ic} is obtained with the largest t value of 10^9 fs, same as for Cu_3 and the Lorentzian broadening of 4×10^{-4} cm⁻¹. The results, also reported in Table IV, reveal that the k_{ic} constant decreases with the increase of the transition energy, ΔE . In addition, the k_{ic} values of the Cu_6 are generally larger than those for Cu_3 . The graphical presentation of k_{ic} diagonal matrix elements is shown in Figure 6, together with the displacement vectors of the normal modes. For this cluster, the geometry displacement, as a result of the one electron excitation, is not always correlated to the normal mode displacement belonging to the highest peak. In addition, only some normal modes have a relevant contribution to the k_{ic} values, and some vibrational normal mode can couple to several excitations with a large IC rate constant. As an example, the mode at 255.32 cm⁻¹ contributes to the k_{ic} values of the excitations 4, 95, and 129 (see Figures 6(b), 6(d), and 6(f)). However, analogously to Cu_3 structure, one promoting mode can be identified at $\nu = 195.15$ cm⁻¹.

An interconversion process has been assigned to the absorption mode at 2.84 eV of Cu_3 cluster, resulting from the acute to obtuse C_{2v} geometry transformation, being induced by the photolysis.²⁹ The formation of a new copper particle, denoted as Cu_3' in this early study, was proposed from the appearance of another peak at 2.60 eV, also interpreted as an interconversion. Our computations did not yield a large probability for interconversion processes in the UV-visible energy range for Cu_3 cluster. Instead, the large k_{ic} value is found for the transitions at 2.75 eV of Cu_6 , being very close to the peak associated with an interconversion in the work of Ozin *et al.*²⁹ It is worth to note that both Cu_3 and Cu_6 species exhibit planar triangular geometry and show very similar optical features. The difficulties to exactly distinguish between various cluster sizes and structures in the rare-gas matrix experiments from the optical spectra analyses are well known and it has been recently emphasized.²³

For the Cu_9 species, we report two values of the k_{ic} constant belonging to the transitions at 1.26 eV and 2.51 eV (see Table IV). These values were obtained without convergence problems and without inclusion of a dephasing factor

(Lorentzian broadening). As can be seen from Table IV, the results reveal that the k_{ic} value of $0.2 \times 10^7 \text{ s}^{-1}$ is considerably higher than the corresponding one at 2.51 eV ($0.3 \times 10^1 \text{ s}^{-1}$) but is less than two orders of magnitude of the k_{ic} value at 2.75 eV ($0.1 \times 10^9 \text{ s}^{-1}$) of the Cu_6 species. From the diagonal matrix elements shown in Figure 7, it follows that several vibrational normal modes couple to these electronic transitions. We can thus conclude that starting with Cu_9 the promoting mode concept becomes obsolete and it is necessary to take into account the Duschinsky mixing effect.

H_2 hot electron photoinduced dissociation

We have chosen to test the application of IC rate constant computations also to the H_2 dissociation on Cu_3 particles. Recent studies demonstrated the energetical benefits of using plasmon-driven dissociation of H_2 on noble metal surfaces by generation of hot electrons.^{71,72} Indeed, the plasmon-driven catalysis is a very intensively developing field of research in the recent years. Hydrogen dissociation on gold nanoparticles, supported on SiO_2 ,⁷² was shown to occur faster by two orders of magnitude than on the same samples, but without using hot electron induced photodissociation. Due to the high energy of the hot electrons, they can extend further away from the noble or transition metal structures transferring into the electronic states of an electron acceptor. An important decrease of the H_2 dissociation energy barrier was obtained also computationally, using correlated wavefunction methods to describe the excited-state potential energy surfaces in order to model hot electron induced photodissociation on Au(111) surface.⁷³

The method to compute the IC rate constant allows us to identify the vibrational mode(s) that would couple with the electronic transition(s) from the occupied MO in the metal cluster to an electron acceptor in the adsorbate, giving rise to the largest value(s) of k_{ic} . This information can be further used to tune the energy of the hot electron as a function of particle size and/or their composition. To prove this concept and to test the validity of the k_{ic} method, we have computed the IC rate constant for the H_2 dissociation on a small Cu_3 particle. Nevertheless, the chosen metal cluster model is small in order to speed up the computations, we estimated it sufficient to obtain qualitative indication about the computational performance of the k_{ic} algorithm and its potential extension to applications in the field of plasmon-induced catalysis.

All the electronic transitions, considered by us, are those between occupied MOs with sp -character of the copper cluster and the empty orbitals with predominant σ^* character of physisorbed H_2 excited states. The excited states' optimized geometries are shown in Figure 8. The matrix elements of k_{ic} are plotted as a function of the vibrational normal modes in Figure 8 as well, and their values are collected in Table V. The IC rate constants were obtained without convergence problems and without inclusion of a dephasing factor (Lorentzian broadening). The vibrational mode assignment is the following: (1) the vibrations at 95.23, 175.11, and 310.57 cm^{-1} correspond to H_2 frustrated translation (out of plane and in plane) and frustrated rotation, respectively; (2) modes with frequencies at 145.09, 166.88, and 244.86 cm^{-1} are the Cu–Cu stretching vibrations; and (3) the Cu–H symmetric and asymmetric stretching and the H–H stretching are located at 703.81,

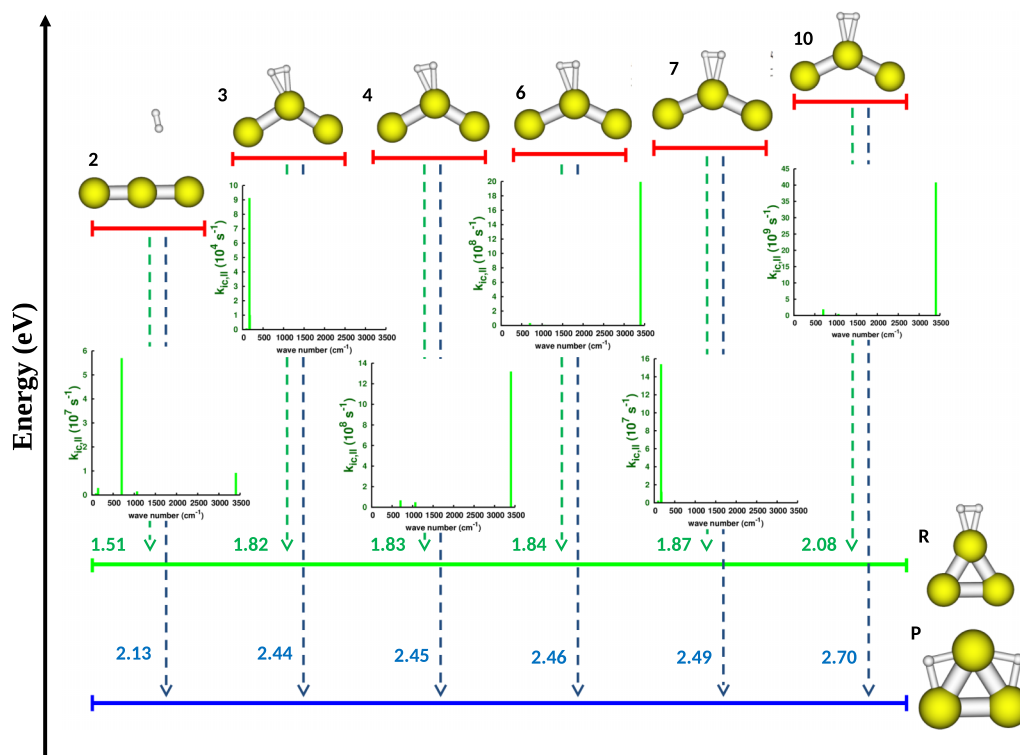


FIG. 8. Graphical representation of the diagonal matrix elements ($k_{il,ic}$) belonging to each frequencies of the H_2/Cu_3 reference ground state. Energy differences between the excited and the ground states are also reported.

TABLE V. Diagonal matrix elements of the k_{ic} rate (s^{-1}) at 300 K of the H_2/Cu_3 .

Frequency (cm^{-1})	State N					
	2	3	4	6	7	10
95.23	0.7×10^6	0.9×10^3	0.8×10^5	0.8×10^6	0.2×10^7	0.5×10^6
145.09	0.3×10^7	0.2×10^3	0.6×10^7	0.3×10^7	0.3×10^6	0.3×10^7
166.88	0.2×10^4	0.9×10^5	0.2×10^4	0.2×10^5	0.2×10^9	0.3×10^6
175.11	0.2×10^6	0.1×10^5	0.3×10^6	0.7×10^5	0.1×10^8	0.3×10^4
244.86	0.1×10^6	0.2×10^2	0.8×10^5	0.1×10^7	0.3×10^5	0.2×10^8
310.57	0.2×10^5	0.2×10^3	0.7×10^5	0.6×10^4	0.4×10^5	0.3×10^6
703.81	0.6×10^8	0.1×10^1	0.7×10^8	0.3×10^8	0.9×10^3	0.2×10^{10}
1066.94	0.2×10^7	0.2×10^1	0.5×10^8	0.9×10^7	0.1×10^5	0.5×10^9
3401.28	0.9×10^7	0.2×10^0	0.1×10^{10}	0.2×10^{10}	0.1×10^3	0.4×10^{11}
k_{ic}	0.7×10^8	0.1×10^6	0.2×10^{10}	0.2×10^{10}	0.2×10^9	0.4×10^{11}

1066.94 and 3401.28 cm^{-1} , respectively. A graphical presentation attempting to visualize these modes is reported in the supplementary material, Figure S14.⁷⁴ The excitation energies, ΔE , of the optimized excited states' structures range from 1.51 eV to 2.08 eV with respect to H_2/Cu_3 . As expected, the dissociated state with two atomically chemisorbed H-atoms on the same Cu-center is more stable than the physisorbed intact hydrogen molecule. Both structures are reported for completeness in Figure 8.

The results reveal that only one excited state couples to several vibrational modes involving the adsorbed H_2 molecule. This is the case of the 2-nd state where the highest intensity is associated to the Cu-H stretching mode at 703.81 cm^{-1} ($0.6 \times 10^8 cm^{-1}$) (see Table V). A coupling leading to a fastest internal conversion (of the order of 10^{11}) is found between the electronic excitation at high energy (2.08 eV) and the H-H stretching at 3401.28 cm^{-1} . This excitation is given by the highest c^2 contribution (80.7%) of the transition involving the HOMO built of sp copper orbitals and LUMO+1 with the σ^* H_2 character. In this case, there is no mixture of vibrational modes. It follows that the simplified picture of only one promoting mode governing the H_2 dissociation is confirmed by the k_{ic} calculations for this small copper cluster and the IC processes involving more normal modes occur only at lower k_{ic} values.

CONCLUSIONS

In this study, we present computations of non-radiative internal conversion rate constants in small copper clusters with three, six, and nine atoms and in the H_2 -adsorbed on Cu_3 cluster as case examples. The IC rate constant can give indications for the probability of the interactions between excited electrons and the vibrational states of the clusters, thus allowing to identify the most probable relaxation pathways in the hot-electron induced photophysics. For these results, we have developed a computer program, based on the method including Duschinsky mixing effect, initially proposed to quantify IC processes in organic molecules.⁴¹⁻⁴⁴

Before proceeding with the IC rate constant calculations, an extensive analysis of the quality of the electronic structures and TDDFT optical spectra depending on the exchanged-

correlation functional and basis set was carried out. The results demonstrated clearly that MOs energies shift down to the lower energies with the increase of the basis set size and of the hybrid part within the exchange correlation functional. The same analysis, performed over the different MO contributions involved in vertical excitations, shows that the PBE functional favours the d character. This effect is decreased by the amount of the hybrid contribution included in the exchange correlation functional. The opposite situation occurs for the s character. Comparison with experimental spectra²³ shows that neither level of theory compares exactly. It is worth noting that a difficulty to compare with experimental results is not only due to the particular computational method but also due to the co-existence under experimental conditions of low-energy copper clusters with same size, but different topologies.

The k_{ic} values predict a fast internal conversion rate processes only in Cu_6 cluster. There is only one vibrational mode resulting to a large k_{ic} value due to its interaction with excited electrons in Cu_3 and Cu_6 , whereas a mixing of vibrational modes is found to play a role in the IC processes in Cu_9 structure. The internal conversion rate, evaluated for a series of excited electronic states in H_2-Cu_3 system, in the range between 1.51 eV and 2.08 eV, is analysed in order to describe the non-radiative photodissociation of H_2 . The fast electron relaxation occurs when the H-H vibrational mode couples to the excitations involving mainly the transition between a MO of the Cu_3 with sp character and the σ^* of the H_2 . The main conclusion is that the excited electrons relax strongly to the H-stretching mode, which correlates with the expectations from the proposed mechanism for the photodissociation of H_2 on noble metal surfaces. Our results predicted also that the H_2 dissociation on a Cu_3 cluster would be predominantly driven by the higher electronic energy transitions at 2.08 eV. Finally, the need to include the Duschinsky mixing effect in the description of the IC process is emphasized.

ACKNOWLEDGMENTS

The financial support from ANR TAR-G-ED is acknowledged. Part of the calculations was performed at the HPC resources of CINES under the allocation x2014086396 made by GENCI (Grand Equipement National de Calcul Intensif). We are grateful to Dr. Ying-Li Niu and Professor Zhigang

Shuai for the fruitful discussions and the practical advices during the computer program preparation, kindly provided by Dr. Ying-Li Niu.

- ¹W. Jahn, *J. Struct. Biol.* **127**, 106 (1999).
- ²K. S. Amankwah and U. De Boni, *Exp. Cell Res.* **210**, 315 (1994).
- ³H. He, C. Xie, and J. Ren, *Anal. Chem.* **80**, 5951 (2008).
- ⁴G. J. Hutchings and R. A. Joffe, *Appl. Catal.* **20**, 215 (1986).
- ⁵Y. Zhu, H. Qian, B. A. Drake, and R. Jin, *Angew. Chem., Int. Ed.* **49**, 1295 (2010).
- ⁶M. Haruta, N. Yamada, T. Kobayashi, and S. Iijima, *J. Catal.* **115**, 301 (1989).
- ⁷U. Heiz and W.-D. Schneider, *J. Phys. D: Appl. Phys.* **33**, R85 (2000).
- ⁸N. Lopez and J. K. Nørskov, *J. Am. Chem. Soc.* **124**, 11262 (2002).
- ⁹A. A. Herzing, C. J. Kiely, A. F. Carley, P. Landon, and G. J. Hutchings, *Science* **321**, 1331 (2008).
- ¹⁰C. Guarise, F. Manea, G. Zaupa, L. Pasquato, L. J. Prins, and P. Scrimin, *J. Pept. Sci.* **14**, 174 (2008).
- ¹¹M. F. Jarrold and K. M. Creegan, *Chem. Phys. Lett.* **166**, 116 (1990).
- ¹²J.-Y. Bigot, J.-C. Merle, O. Cregut, and A. Daunois, *Phys. Rev. Lett.* **75**, 4702-4705 (1995).
- ¹³B. A. Smith, J. Z. Zhang, U. Giebel, and G. Schmid, *Chem. Phys. Lett.* **270**, 139-144 (1997).
- ¹⁴Y. Takeda, J. P. Zhao, C. G. Lee, V. T. Gritsyna, and N. Kishimoto, *Nucl. Instrum. Methods Phys. Res., Sect. B* **166-167**, 877-881 (2000).
- ¹⁵J. H. Hodak, A. Henglein, and G. V. Hartland, *J. Phys. Chem. B* **104**, 9954 (2000).
- ¹⁶S. Link, M. A. El-Sayed, T. G. Schaaff, and R. L. Whetten, *Chem. Phys. Lett.* **356**, 240-246 (2002).
- ¹⁷C. Voisin, D. Christofilos, P. A. Loukakos, N. Del Fatti, and F. Vallee, *Phys. Rev. B* **69**, 195416 (2004).
- ¹⁸C. D. Grant, A. M. Schwartzberg, Y. Yang, S. Chen, and J. Z. Zhang, *Chem. Phys. Lett.* **383**, 31-34 (2004).
- ¹⁹L. D. Petanza, G. Colonna, S. Longo, and M. Capitelli, *Eur. Phys. J. D* **45**, 369-389 (2007).
- ²⁰D. B. Pedersen and S. Wang, *J. Phys. Chem. C* **111**, 17493-17499 (2007).
- ²¹M. Hu, J. Y. Chen, Z. Y. Li, L. Au, G. V. Hartland, X. D. Li, M. Marquez, and Y. N. Xia, *Chem. Soc. Rev.* **35**, 1084 (2006).
- ²²G. V. Hartland, *Chem. Rev.* **111**, 3858-3887 (2011).
- ²³S. Lecoultré, A. Rydlo, C. Félix, J. Buttet, S. Gilb, and W. Harbich, *J. Chem. Phys.* **134**, 074303 (2011).
- ²⁴M. Zaaour, B. Dong, I. Naydenova, R. Retoux, and S. Mintova, *Microporous Mesoporous Mater.* **189**, 11-21 (2014).
- ²⁵C. F. Bohren and D. R. Huffman, *Absorption and Scattering of Light by Small Particles* (Wiley, New York, 1983).
- ²⁶E. J. Zeman and G. C. Schatz, *J. Phys. Chem.* **91**, 634 (1987).
- ²⁷M. Vollmer and U. Kreibig, *Optical Properties of Metal Clusters* (Springer, New York, 1994).
- ²⁸G. Celep, E. Cottancin, J. Lermé, M. Pellarin, L. Arnaud, J. R. Huntzinger, J. L. Vialle, M. Broyer, B. Palpant, O. Boisron, and P. Mélinon, *Phys. Rev. B* **70**, 165409 (2004).
- ²⁹G. A. Ozin, S. A. Douglas, F. McIntosh, S. M. Mattar, and J. Garcla-Prieto, *J. Phys. Chem.* **87**, 4651-4665 (1983).
- ³⁰G. Mie, *Ann. Phys. (Weinheim, Ger.)* **330**, 377 (1908).
- ³¹S. Link and M. A. El-Sayed, *Int. Rev. Phys. Chem.* **19**, 409 (2000).
- ³²A. Baiardi, J. Bloino, and V. Barone, *J. Chem. Theory Comput.* **9**, 4097-4115 (2013).
- ³³H.-C. Jankowiak, J. L. Stuber, and R. Berger, *J. Chem. Phys.* **127**, 234101 (2007).
- ³⁴V. Barone, J. Bloino, M. Biczysko, and F. Santoro, *J. Chem. Theory Comput.* **5**, 540-554 (2009).
- ³⁵T. Petrenko and F. Neese, *J. Chem. Phys.* **127**, 164319 (2007).
- ³⁶T. Petrenko and F. Neese, *J. Chem. Phys.* **137**, 234107 (2012).
- ³⁷D. W. Silverstein and L. Jensen, *J. Chem. Phys.* **136**, 064110 (2012).
- ³⁸R. Ianculescu and E. Pollak, *J. Phys. Chem. A* **108**, 7778-7784 (2004).
- ³⁹J. Tatchen and E. Pollak, *J. Chem. Phys.* **128**, 164303 (2008).
- ⁴⁰J. Tang, M. T. Lee, and S. H. Lin, *J. Chem. Phys.* **119**, 7188-7196 (2003).
- ⁴¹Y. Niu, Q. Peng, and Z. Shuai, *Sci. China, Ser. B: Chem.* **51**, 1153 (2008).
- ⁴²Y. Niu, Q. Peng, C. Deng, X. Gao, and Z. Shuai, *J. Phys. Chem. A* **114**, 7817-7831 (2010).
- ⁴³Q. Wu, Q. Peng, Y. Niu, X. Gao, and Z. Shuai, *J. Phys. Chem. A* **116**, 3881 (2012).
- ⁴⁴Q. Peng, Y. Niu, C. Deng, and Z. Shuai, *Chem. Phys.* **370**, 215-222 (2010).
- ⁴⁵J. Franck, *Trans. Faraday Soc.* **21**, 536-542 (1926).
- ⁴⁶J. Franck, F. Weigert, H. v. Halban, M. Bodenstein, E. C. C. Baly, B. Lewis, D. L. Chapman, H. S. Taylor, A. J. Allmand, J. A. Christiansen, E. J. Bowen, W. A. Noyes, O. Stern, R. G. W. Norrish, B. Flurscheim, and A. L. Marshall, *Trans. Faraday Soc.* **21**, 581-590 (1926).
- ⁴⁷E. U. Condon, *Phys. Rev.* **28**, 1182-1201 (1926).
- ⁴⁸E. U. Condon, *Phys. Rev.* **32**, 858-872 (1928).
- ⁴⁹G. Herzberg and E. Teller, *Z. Phys. Chem., Abt. B* **21**, 410-446 (1933).
- ⁵⁰F. Duschinsky, *Acta Physicochim. URSS* **7**, 551 (1937).
- ⁵¹K. Shizu, T. Sato, and K. Tanaka, *Nanoscale* **2**, 2186 (2010).
- ⁵²Y. He and E. Pollak, *J. Chem. Phys. A* **105**, 10961-10966 (2001).
- ⁵³E. Pollak and L. J. Liao, *J. Chem. Phys.* **108**, 2733-2743 (1998).
- ⁵⁴J. Shao, L. J. Liao, and E. Pollak, *J. Chem. Phys.* **108**, 9711-9725 (1998).
- ⁵⁵J. Tang and S. H. Lin, *Phys. Rev. E* **73**, 061108-061110 (2006).
- ⁵⁶R. Send and F. Furche, *J. Chem. Phys.* **132**, 044107 (2010).
- ⁵⁷TURBOMOLE V6.4, a development of University of Karlsruhe and Forschungszentrum Karlsruhe GmbH, 1989-2007, TURBOMOLE GmbH, since 2007, available from <http://www.turbomole.com>.
- ⁵⁸A. Schafer, H. Horn, and R. Ahlrichs, *J. Chem. Phys.* **97**, 2571 (1992).
- ⁵⁹F. Weigend and R. Ahlrichs, *Phys. Chem. Chem. Phys.* **7**, 3297 (2005).
- ⁶⁰J. P. Perdew, K. Burke, and M. Ernzerhof, *Phys. Rev. Lett.* **77**, 3865 (1996).
- ⁶¹A. D. Becke, *J. Chem. Phys.* **98**, 5648 (1993).
- ⁶²C. Lee, W. Yang, and R. Parr, *Phys. Rev. B* **37**, 785 (1988).
- ⁶³J. P. Perdew, M. Ernzerhof, and K. Burke, *J. Chem. Phys.* **105**, 9982 (1996).
- ⁶⁴W. Koch and M. C. Holthausen, *A Chemist's Guide to Density Functional Theory*, 2nd ed. (Wiley-VCH Verlag GmbH, Berlin, 2001), p. 134.
- ⁶⁵K. Jug, B. Zimmermann, P. Calaminici, and A. M. Köster, *J. Chem. Phys.* **116**, 4497 (2002).
- ⁶⁶P. Calaminici, A. M. Köster, and Z. Gomez-Sandoval, *J. Chem. Theory Comput.* **3**, 905 (2007).
- ⁶⁷G. H. Guvelioglou, P. Ma, X. He, R. C. Forrey, and H. Cheng, *Phys. Rev. B* **73**, 155436 (2006).
- ⁶⁸P. Jaque and A. Toro-Labbe, *J. Chem. Phys.* **117**, 3208 (2002).
- ⁶⁹M. Yang, K. A. Jackson, C. Koehler, T. Frauenheim, and J. Jellinek, *J. Chem. Phys.* **124**, 024308 (2006).
- ⁷⁰W.-D. Hsu, M. Ichihashi, T. Kondow, and S. B. Sinott, *J. Chem. Phys.* **124**, 024308 (2006).
- ⁷¹S. Mukherjee, F. Libisch, N. Large, O. Neumann, L. V. Brown, J. Cheng, B. Lassiter, E. A. Carter, P. Nordlander, and N. J. Halas, *Nano Lett.* **13**, 240 (2013).
- ⁷²S. Mukherjee, L. Zhou, A. M. Goodman, N. Large, C. Ayala-Orozco, Y. Zhang, P. Nordlander, and N. J. Halas, *J. Am. Chem. Soc.* **136**, 64 (2014).
- ⁷³F. Libisch, J. Cheng, and E. A. Carter, *Z. Phys. Chem.* **227**, 1455 (2013).
- ⁷⁴See supplementary material at <http://dx.doi.org/10.1063/1.4915127> for more details on the density of state spectra for the considered copper clusters, vertical excitations, molecular orbital plots, and vibrational displacement vectors.